AMERICAN METEOROLOGICAL SOCIETY

Journal of Physical Oceanography

EARLY ONLINE RELEASE

The DOI for this manuscript is doi: 10.1175/JPO-D-17-0022.1

Generation of sub-surface anticyclones at Arctic surface fronts due to a surface stress

Liam Brannigan*

Dept. of Meteorology, Stockholm University, Sweden

Helen Johnson

Earth Sciences, University of Oxford, UK

Camille Lique

Laboratoire d'Oceanographie Physique et Spatiale, UMR 6523,

CNRS-IFREMER-IRD-UBO, Brest, France

Jonas Nycander and Johan Nilsson

Dept. of Meteorology, Stockholm University, Sweden

Corresponding author address: Liam Brannigan, Dept. of Meteorology, Stockholm University, Sweden.

E-mail: liam.brannigan@misu.su.se

ABSTRACT

Isolated anticyclones are frequently observed below the mixed layer in the Arctic Ocean. Some of these sub-surface anticyclones are thought to originate at surface fronts. However, previous idealized simulations with no surface stress show that only cyclone-anticyclone dipoles can propagate away from baroclinically unstable surface fronts. Numerical simulations of fronts subject to a surface stress presented here show that a surface stress in the same direction as the geostrophic flow inhibits dipole propagation away from the front. On the other hand, a surface stress in the opposite direction to the geostrophic flow helps dipoles to propagate away from the front. Regardless of the surface stress at the point of dipole formation, these dipoles can be broken up on a timescale of days when a surface stress is applied in the right direction. The dipole breakup leads to the deeper anticyclonic component becoming an isolated sub-surface eddy. The breakup of the dipole occurs because the cyclonic component of the dipole in the mixed layer is subject to an additional advection due to the Ekman flow. When the Ekman transport has a component oriented from the anticyclonic part of the dipole towards the cyclonic part then the cyclone is advected away from the anticyclone and the dipole is broken up. When the Ekman transport is in other directions relative to the dipole axis it also leads to deviations in the trajectory of the dipole. A scaling is presented for the rate at which the surface cyclone is advected that holds across a range of mixed layer depths and surface stress magnitudes in these simulations. The results may be relevant to other regions of the ocean with similar near-surface stratification profiles.

1. Introduction

Isolated anticyclones below the base of the mixed layer are frequently observed in the Canadian Basin of the Arctic Ocean (Newton et al. 1974; Hunkins 1974; Manley and Hunkins 1985; D'Asaro 1988; Padman et al. 1990; Plueddemann et al. 1998; Pickart et al. 2005; Timmermans et al. 2008; Zhao et al. 2014; Zhao and Timmermans 2015), but their formation mechanism is unclear. Timmermans et al. (2008) and Zhao et al. (2014) find that the hydrographic properties of these eddies are consistent with formation of the eddies at a surface front under sea-ice near 78-80°N. This front is associated with the lateral expansion of the fresh Pacific Water into the saltier surface water on the Eurasian side of the Arctic Ocean. The front has been shown to change location in response to changes of the large scale atmospheric circulation over the Arctic (Steele et al. 2004; Alkire et al. 2007).

Zhao et al. (2014) perform a survey of halocline eddies in the Canada Basin observed with ice-tethered profilers, an example of which is shown in Fig. 1. They find that the halocline eddies have a typical length scale L comparable to the first baroclinic Rossby radius of deformation. This property corresponds to the halocline eddies having Bu ≈ 1, where Bu$= R_d/L$ is the Burger number, and deformation radii of around 10 km. The eddies are in cyclogeostrophic balance with maximum azimuthal velocities of 0.05 to 0.4 m s^{-1}. Zhao et al. (2016) show that anticyclonic eddies account for 98% of the observed halocline eddies in the Arctic. Zhao et al. (2014) find that there are four categories of halocline eddies: shallow and deep Canadian Water eddies as well as shallow and deep Eurasian Water eddies. Zhao et al. (2014) define 'shallow' in this case to mean eddies with a core that is shallower than 80 m depth. The generation of the shallow Canadian Water and Eurasian Water anticyclonic eddies is the main focus of this work.

Manucharyan and Timmermans (2013) carry out a set of idealized numerical experiments of the instabilities of a surface front with characteristics similar to those of the mixed layer front observed by Timmermans et al. (2008). Manucharyan and Timmermans (2013) find that baroclinic instability leads to the formation of cyclone-anticyclone dipoles that can self-propagate away from the original front. They find, however, that these dipoles tend to follow curved paths that eventually take them back to the original front.

The simulations presented here depart from those of Manucharyan and Timmermans (2013) primarily in that a surface stress is employed to account for momentum transfer to or from the ocean. There are two central hypotheses in this work. The first hypothesis is that dipole propagation away from baroclinically unstable surface fronts is aided by a surface stress opposed to the geostrophic current and inhibited by a surface stress aligned with the geostrophic current. The second hypothesis is that the Ekman transport can lead to the breakup of dipoles by advecting the surface cyclonic component away from the sub-surface anticyclonic component. Section 2 describes the experimental set-up and Section 3 describes dipole formation and subsequent breakup for simulations carried out with a constant surface stress. This mechanism for dipole breakup is explored further in Section 4 with a hierarchy of models. A summary and discussion follow in Section 5.

2. Experimental set-up

a. Overview

The domain used for all experiments is a doubly-periodic box with a meridional length of 384 km, a zonal length of 64 km and a depth of 90 m (Fig. 2). As for Manucharyan and Timmermans (2013), the initial conditions are motivated by observations of a near-surface front in the Arctic near 80°N (Timmermans et al. 2008). There is a region of fresher, lighter fluid in the center

of the domain that overlies and is bounded on the northern and southern sides by saltier, denser fluid. This set-up gives rise to two fronts with geostrophic flow in opposite directions (Fig. 2). As is typical for such idealized simulations (e.g. Fox-Kemper et al. 2008), it is assumed that the fronts were created by the straining action of a larger-scale flow field that is not captured in these experiments. This model set-up is similar to that used by Thomas (2008), though modified to reflect an idealized Arctic configuration where the Coriolis parameter $f = 1.4 \times 10^{-4}$ s^{-1} rather than a mid-latitude open ocean configuration.

The mixed layer deformation radius $R_{\mathrm{ML}} \approx \sqrt{\delta b H_{\mathrm{ML}}}/f \approx 4$ km, where δb is the buoyancy contrast across the front and H_{ML} is the mixed layer depth. The mixed layer depth is taken to be the shallowest depth where the salinity is 0.4 psu greater than at the surface. Given this small deformation radius relative to the 180 km spacing between the two fronts the experiment set-up should be thought of as two independent fronts rather than as a system of two coupled fronts. The zonal length of the domain is set to be long enough for multiple baroclinic waves to develop. The depth of the domain is chosen to allow the presence of a surface front without strong bottom friction effects. As the domain is doubly periodic a uniform surface stress can be applied without requiring tapering of the surface stress at the domain boundaries. This is an advantage as such tapering gives rise to spurious Ekman pumping. The overall numerical set-up is set out below before the particular parameters for each experiment are given in Section 2e.

b. Numerical configuration

The simulations are carried out using the MITgcm in hydrostatic mode (Marshall et al. 1997). A comparison is made of results with model horizontal grid resolutions of 1 km, 0.5 km and 0.25 km. The grid spacing for all runs in the vertical is 0.5 m in the upper 25 m and increases gradually to 1.5 m towards the base of the domain. The model time step is 25 s at 0.25 km grid spacing and

the timestep scales in a 1:1 ratio with changes in the horizontal grid spacing. The code used to generate the model inputs is made available online as set out in the Acknowledgments.

The model is run with the vector invariant form of the momentum equation. Biharmonic operators are used in the horizontal for both viscosity and diffusivity as these target dissipation at the shortest scales (Griffies and Hallberg 2000; Graham and Ringler 2013). While a constant horizontal diffusivity coefficient of 10^3 m^4 s^{-1} is used for salinity, the horizontal viscosity is set using a Smagorinsky scheme (Smagorinsky 1963) with a coefficient of 1 to allow submesoscale features to develop (Ilicak et al. 2012; Graham and Ringler 2013; Ramachandran et al. 2013). Laplacian operators are used in the vertical with viscous and diffusive parameters of 10^{-5} m^2 s^{-1}.

A 7th-order monoticity preserving tracer advection scheme (Daru and Tenaud 2004) is used to maintain submesoscale structures. The *K* Profile Parameterization (*KPP*) scheme (Large et al. 1994) is used to parameterize surface boundary layer turbulence. This scheme captures the dynamics of a shear-driven boundary layer such as that found underneath sea-ice. No surface buoyancy flux or explicit sea ice model is used.

c. Initial conditions

The initial conditions depart from those of Manucharyan and Timmermans (2013) in that the domain is mirrored in the meridional direction to give two fronts of opposite orientation (Fig. 2) and that the deeper stratification is omitted. The initial distribution of the salinity field S for the southern front is

$$S = S_0 - \left[\frac{\mathrm{dSh}}{4} \left(1 + \tanh\left(\frac{z + H_{\mathrm{strat}}}{\mathrm{dH}} \right) \right) \left(1 + \tanh\left(\frac{(2L/3) - y}{L_f} - 1 \right) \right) \right] \tag{1}$$

where (y, z) are the meridional and vertical coordinates, S_0 is the reference salinity, dSh is the horizontal salinity difference across the front, H_{strat} is the stratification depth, dH is the vertical

stratification thickness, L is half the meridional length of the final domain and L_f is the frontal width.

As H_{strat} is the depth of peak stratification, it will always be larger than the mixed layer depth. In practice we find that the mixed layer depth $H_{\text{ML}} \approx H_{\text{strat}} - \text{dH}$. This linear relationship means that results presented below as scaling with the stratification depth can equivalently be thought of as scaling with the mixed layer depth. The range of parameters used to set the initial and boundary conditions is set out in Table 1.

The salinity distribution is used to set the potential density ρ based on a linear equation of state with a saline coefficient of $\beta = 7.4\times10^{-4}$ psu^{-1} and with no thermal component. As such the buoyancy anomaly $b = -g\beta(S - S_0)$, where $g = 9.81$ m s^{-2} is gravitational acceleration and $S_0 = 31$ psu. Once the potential density field is calculated, the free surface elevation η is set so that there is no bottom pressure perturbation:

$$\eta(y) = \frac{1}{\rho_0}\int_{-D}^{0} \rho(y,z) - \frac{1}{2}[\rho(0,z) + \rho(L,z)]dz \tag{2}$$

where ρ_0 is a reference potential density and D is the domain depth. Given that there is zero pressure perturbation and zero flow at the bottom, the initial zonal geostrophic velocity is given by integrating the thermal wind relation upwards:

$$u(y,z) = \frac{g}{f}\int_{-D}^{z} \frac{1}{\rho_0}\frac{\partial \rho}{\partial y}dz. \tag{3}$$

A white noise random perturbation of amplitude 10^{-3} m s^{-1} is added to the initial velocity field to allow instabilities to grow. The magnitude of this random perturbation decreases exponentially with depth from the surface with a decay length scale of the stratification depth H_{strat}.

d. Boundary conditions

Simulations are carried out both with and without a surface stress to allow the results to be compared with previous work. Firstly, there are simulations with no surface stress i.e.

$$K_z \frac{\partial \mathbf{u}_h}{\partial z} = (0,0), \quad z = 0 \tag{4}$$

where K_z is the vertical viscosity, $\mathbf{u}_h$ is the horizontal velocity vector and this experiment is referred to as 'NoStress'. This is the surface boundary condition used by Manucharyan and Timmermans (2013). While there is no vertically-integrated Ekman transport in the simulations with no surface stress, there is an ageostrophic boundary layer flow that arises to satisfy the no stress boundary condition in the presence of thermal wind shear (Wenegrat and McPhaden 2016).

Secondly, there are simulations with a spatially uniform surface stress i.e.

$$K_z \frac{\partial \mathbf{u}}{\partial z} = \frac{1}{\rho_0}(\tau_x, \tau_y), \quad z = 0 \tag{5}$$

where $\tau = (\tau_x, \tau_y)$ represents the net surface stress exerted by the wind and sea ice motion on the ocean surface. The magnitude and direction of this stress differs between experiments, as described below.

The surface stress is increased linearly from 0 to its final value over the course of the first days of the simulations to reduce the generation of inertial oscillations. Additional experiments with a surface stress applied instantaneously shows that these inertial oscillations have no effect on the eddy generation process, but make visualization of the process more difficult.

The bottom boundary condition is partial slip with a non-dimensional quadratic drag coefficient of 3×10^{-3}. The lateral boundary condition is periodic in both horizontal directions.

e. Non-dimensional parameters

Mahadevan et al. (2010) show that the relative importance of restratification driven by the Ekman transport versus eddy-driven restratification is given by the ratio

$$r = \frac{\tau/\rho f}{0.06 H_{ML}^2 |\nabla_h^2 b|/f}. \tag{6}$$

The numerator of this ratio is the magnitude of the Ekman transport streamfunction while the denominator is the magnitude of the streamfunction due to mixed layer baroclinic instability from the Fox-Kemper et al. (2008) parameterization. For the Base experiment here $r = 1.3$, suggesting that both surface stress-driven restratification and eddy-driven restratification are important.

A key non-dimensional parameter for understanding the stability of submesoscale fronts is the balanced Richardson number

$$\mathrm{Ri} = f^2 N^2 / M^4 \tag{7}$$

where $M^4 = |\nabla_h b|^2$ is the square of the horizontal buoyancy gradient and $N^2 = b_z$ is the vertical buoyancy gradient. Timmermans et al. (2012) show that $1 < \mathrm{Ri} < 10$ is a representative range for surface fronts observed with ice-tethered profilers in wintertime in the Canada Basin. We carry out experiments where Ri is varied over a range of values to understand the effect of changing Ri on eddy generation. Since Ri varies across the front the value given in Table 1 is the mean over the frontal region in the mixed layer with lower values found in the center of the front where the lateral gradients are strongest.

f. Base experiments

The Base experiments have the same surface stress applied throughout (apart from the initial spin-up phase of 3 days). These experiments are carried out at 0.25 km resolution and have $H_{\mathrm{strat}} = 30$ m (Table 1) that is a representative value from observations under sea ice (Timmer-

mans et al. 2012). The magnitude of τ_x is 0.03 N m^{-2} for the Base experiment, typical of the root-mean-square stress on the Arctic Ocean under sea ice (Martin et al. 2014). The sensitivity to these parameters is tested by running additional simulations with varying horizontal grid resolution, surface stress magnitude and cross-front salinity difference (Table 1). These simulations are integrated for 75 days. The stratification thickness is dH= 5 m and the frontal width is $L_f = 10$ km for all experiments.

g. Restart experiments

In order to test the hypothesis for eddy generation developed in the Base experiments, further experiments are carried out and are referred to as the 'Restart' experiments. The set-up for these experiments is described in Section 4.

h. Ekman depth

With constant vertical viscosity K_z the Ekman depth $H_{\mathrm{Ek}} = \sqrt{K_z/f}$. However, this scaling is not readily applicable here as the *KPP* scheme leads to large variations of the vertical viscosity through the mixed layer. The Ekman depth is instead diagnosed from the simulations as the vertical e-folding lengthscale of the magnitude of the ageostrophic flows. The calculation is based on horizontal velocities at a point in the center of the domain – where geostrophic flows are very weak – after six days of the simulations when the Ekman steady state has been reached. The linear regression is carried out using the Scikit-learn package in python (Pedregosa et al. 2011).

For a surface stress of magnitude 0.03 N m^{-2} and stratification depth $H_{\mathrm{strat}} = 30$ m, the Ekman depth is about 10-11 m in these experiments and so is close to the median value of 11 m observed from ice-tethered profilers in the Arctic (Cole et al. 2014). We find that variations in Ekman

layer depth as the surface stress and stratification depth are changed are captured by the scaling $H_{\mathrm{Ek}} \approx 0.3u_*/f$, where the friction velocity $u_* = \sqrt{|\tau|/\rho_0}$.

3. Base experiments

a. No surface stress

For the 'NoStress' simulation with zero surface stress, instability of the surface fronts leads to the formation of cyclone-anticyclone dipoles that propagate away from the front (Fig. 3, a). The cyclonic component of the dipole is stronger near the surface (for example near (27, 125) in Fig. 3, a), while the anticyclonic component is stronger below the mixed layer base (Fig. 3, d). This vertical asymmetry of the dipole is consistent with previous results (e.g. Spall 1995; Manucharyan and Timmermans 2013).

A vertical section through this dipole in the NoStress simulation (Fig. 4, a) confirms that the dipole at $y = 125$ km is formed of tightly coupled vortices of opposite sign. The dipole has a vertical asymmetry as the cyclonic component is stronger closer to the surface than the anticyclonic component.

Dipole structures can have a number of alignments including configurations where the components are arrayed vertically (e.g. Chao and Shaw 1996) or horizontally (e.g. Morel and Thomas 2009). However, dipoles where the components are offset in both the horizontal and vertical – as in this case – have the strongest self-propagation (Hogg and Stommel 1985; Manucharyan and Timmermans 2013). The formation of dipoles with this alignment is likely at restratifying mixed layer fronts as the vortex squashing of fluid particles on the dense side of the fronts creates anticyclones below the base of the mixed layer while the vortex stretching in the mixed layer creates cyclones (Spall 1995).

The dipole in the NoStress experiment follows a curved path that takes it back to the original front (Manucharyan and Timmermans 2013). This curved path is shown by the dots indicating the trajectory of the cyclone and anticyclone in Fig. 3 (a,d). Upon returning to the original front the dipole components merge back into the turbulent frontal field (not shown). Manucharyan and Timmermans (2013) define a kinematic parameter $\omega = (U_2 - U1)/\Delta$ where U_1 is the translation speed of the cyclone, U_2 is the translation speed of the anticyclone and Δ is the distance between the eddy centers. The timescale $2\pi/\omega$ is the time required for the cyclone and anticyclone to orbit each other and so is also a timescale for the length of time that is required for the dipole to return to the front. This timescale is about 12 days in this case.

b. Upfront surface stress

The force balance between the Coriolis acceleration and the downwards transfer of momentum by turbulence leads to an Ekman spiral (Ekman 1905). When the resulting flow is integrated vertically the Ekman spiral leads to an Ekman transport to the right of the surface stress in the northern hemisphere. Where the surface stress is aligned with the geostrophic flow the Ekman transport advects heavier water over lighter water in the Ekman layer. This Ekman transport induces convective mixing and leads to a steepening of isopycnals (Thomas and Rhines 2002; Thomas 2005; Thomas and Lee 2005; Thomas and Ferrari 2008). This scenario of a surface stress aligned with the geostrophic flow is referred to as a 'downfront' stress and can lead to the development of symmetric instability (Thomas 2005; Taylor and Ferrari 2010; Thomas et al. 2013; Brannigan et al. 2015; Brannigan 2016; Buckingham et al. 2016; Thompson et al. 2016). In contrast, where the surface stress is opposed to the geostrophic flow the Ekman transport acts to transport lighter water over heavier water in the Ekman layer. This Ekman transport leads to a restratification in the Ekman layer (Thomas and Rhines 2002; Thomas 2005; Thomas and Lee

2005; Thomas and Ferrari 2008). This scenario of a surface stress opposed to the geostrophic flow is referred to as an 'upfront' stress.

Around day 24 of the Base simulation with an upfront stress, a cyclone-anticyclone dipole propagates northwards from the front. As in the NoStress simulation, this dipole begins by following a curved path (see dots indicating the vortex trajectories in Fig. 3 b,e). However, in the following days the cyclone begins to translate soutwards while the anticyclone moves in a straight line at a decreasing speed (Fig. 3 b,e). This differential advection of the cyclone leads to the breakup of the dipole. The cyclone continues back towards the initial front, while the anticyclone becomes an isolated sub-surface vortex (Fig. 4, b). The dipole formation and breakup under an upfront stress is shown in the accompanying animation.

The southwards advection of the cyclone is in the direction of the Ekman transport. Furthermore, as the Ekman layer depth is about 11 m, only the cyclonic component of the dipole in the mixed layer is affected by the Ekman flow. Our hypothesis is that the dipole breakup occurs due to the effect of the Ekman flow acting on the cyclone. This hypothesis is tested in Section 4 below.

The sub-surface anticyclone under an up-front surface stress is found in the high stratification region below the mixed layer and deforms the base of the mixed layer (Fig. 4, b), consistent with observations of anticyclones below the mixed layer base from the Canada Basin (Fig. 1). This anticyclone has a vertical component of relative vorticity $\zeta^z \approx 0.8f$ (Fig. 4, b) similar to that found in observations (Timmermans et al. 2008; Zhao et al. 2014). The peak flow around this eddy has an amplitude of approximately 5 cm s^{-1}. These magnitudes of azimuthal flow are at the lower end of the range observed in the Arctic (Timmermans et al. 2008; Zhao et al. 2014). Given the similar properties of the observed and simulated eddies, however, it is plausible that some of the observed sub-surface anticyclones are formed by a similar mechanism to the simulated anticyclonic eddies here.

c. Downfront surface stress

For the northern front, with a downfront surface stress, there is a highly turbulent eddy field (Fig. 3, c), similar to the front with no surface stress (Fig. 3, a) though with larger anomalies in ζ^z. There is a strong anticyclonic vorticity anomaly below the base of the mixed layer at $y = 254$ km (Fig. 3, f). However, this anomaly is part of anticyclonic flow that is coherent to the surface (Fig. 4, c) and thus does not have similar properties to the observed eddies. Dipoles do periodically form at the southern, lighter side of this front. However, the ability of these dipoles to self-propagate clear of the front to the south is limited as the frontal outcrop itself is advected southwards at a similar rate. As such, the downfront stress inhibits the formation of dipoles that can propagate away from the front.

d. Sensitivity experiments

We examine the range of applicability of the results of the Base experiments by varying key parameters, as set out in Table 1.

1) VARYING THE GRID RESOLUTION

The Base experiment is run at grid resolutions of 1 km (Base1000), 0.5 km (Base0500) and 0.25 km (Base) (Fig. 5, a-c). At 1 km grid spacing (Fig. 5, a) the formation of sub-surface anticyclones is limited with just a single such eddy at (55,95). The lengthscale of the fastest growing mode of baroclinic instability in the mixed layer as predicted by linear stability analysis (Stone 1966) is:

$$L_s = \frac{2\pi}{k_s} = \frac{2\pi U}{|f|}\sqrt{\frac{1+\mathrm{Ri}}{5/2}} \tag{8}$$

where k_s is the wavenumber of the fastest-growing mode and U is the geostrophic velocity scale. For the initial conditions in the Base experiments $\mathrm{Ri} = 1.8$, $U \approx 0.09$ m s^{-1} and so $L_s \approx 4.3$ km. The relative lack of sub-surface anticyclones at 1 km resolution thus reflects the fact that a grid

resolution of 1 km is marginal for permitting the frontal instabilities and thus energetic dipoles that can escape the frontal region.

The simulations at 0.5 km and 0.25 km (Fig. 5, b-c) produce similar results in that isolated anticyclones of comparable strength are produced at the front subject to an upfront stress, while a turbulent eddy field is produced at the northern front with a downfront stress but without isolated sub-surface anticyclones emerging (not shown). As the results at 0.5 km are much cheaper computationally, the 0.5 km resoluton set-up is used to test further variations in the parameters.

2) VARYING THE SURFACE STRESS

For the HalfStress experiment with $\tau_x = 0.015$ N m^{-2}, the results are more similar to the NoStress experiment as dipoles are not broken up but instead follow curved paths back to their original front for both a downfront (Fig. 6 a) and an upfront (Fig. 6 d) stress. The eddy trajectories are nonetheless affected by the surface stress, as shown in Section 4e below.

When the surface stress is doubled (DoubleStress), the results for a downfront stress (Fig. 6, c) are similar to that for the Base0500 experiment (Fig. 6, b) in that no remote eddies are formed. For a doubled upfront stress, however, a much greater number of sub-surface eddies form for the same length of front (Fig. 6, f).

3) VARYING THE STRATIFICATION DEPTH

When the surface stress is held constant at $\tau_x = 0.03$ N m^{-2} the results change as the stratification depth H_{strat} is varied. For a simulation with a stratification depth of 20 m (labeled $H_{\text{strat}}20$) – corresponding to a mixed layer of approximately 15 m – the Ekman layer extends through almost the entire mixed layer and thus the front subject to an upfront surface stress is largely advected and restratified by the Ekman transport with little role for dynamic instabilities compared to the

main experiment (Fig. 7, a-b). With $H_{\text{strat}} = 20$ m, the parameter $r = 3$ in equation (6) compared to $r = 1.3$ for the Base0500 experiment. As such, the results of this case with shallower stratification depth and $|\tau| = 0.03$ N m^{-2} are consistent with the prediction of restratification dominated by the Ekman transport.

When the stratification depth is deepened to 40 m ($H_{\text{strat}}40$) the parameter $r < 1$ in equation (6). The front subject to an upfront stress again produces isolated anticyclone vortices with this deeper stratification depth (Fig. 7, c). The deeper mixed layer depth in this case leads to a larger mixed layer deformation radius and thus eddies with a larger diameter (Fig. 7, c). At the front subject to a downfront stress the results of the $H_{\text{strat}}20$ and $H_{\text{strat}}40$ simulations are qualitatively similar to those in the Base experiment.

4) VARYING THE FRONTAL STRENGTH

The initial frontal strength is varied by adjusting dSh, the horizontal difference in salinity across the front. Increasing dSh decreases the initial balanced Richardson number (Table 1). Thus, an increase in dSh decreases the length scale of instability by equation (8). In addition, the parameter r in equation (6) predicts that the amount of eddy-driven restratification increases relative to Ekman-driven restratification with increasing values of dSh as there is more available potential energy to drive eddy-driven restratification.

The eddy field becomes stronger as the frontal strength is increased in the simulations under an upfront stress (Fig. 7, d-g). Isolated sub-surface anticyclones form for dSh $\gtrsim 0.75$ psu (Fig. 7, d-f) or Ri $\lesssim 3$. For the simulation with the weakest frontal strength (Fig. 7, d) the eddy field is much weaker and the front is primarily restratified by the Ekman transport. The individual anticyclones have smaller anomalies in ζ^z/f as the frontal strength is reduced.

Instabilities at weaker fronts with higher initial Ri are expected to grow more slowly (Stone 1966) and so a comparison at fixed time (Fig. 7, d-g) occurs at an earlier time point in a non-dimensional sense for the fronts with higher Ri. However, sub-surface eddies do not form at the front with dSh $= 0.5$ at later time points out to day 70 of the simulations (not shown).

For a downfront stress the results are again similar to those found for the main experiment, as dipole propagation is inhibited by the advection of the surface front.

5) Summary of sensitivity experiments

The sensitivity experiments show that the generation of sub-surface anticyclones under an upfront surface stress happens over a wide range of parameter space. Weak surface stress magnitudes lead to results more similar to the dipole propagation in the NoStress experiment. The primary effect of stronger initial fronts or deeper mixed layers is the formation of stronger sub-surface anticyclones. An increasing number of sub-surface anticyclones form for a stronger upfront stress, while the relationship between the number of eddies and the frontal strength and mixed layer depth is less clear. Under a downfront stress the sensitivity experiments show that dipole propagation is possible under a weak surface stress, but the faster advection of the surface front with a stronger surface stress inhibits dipole formation.

4. Restart experiments

The experiments with an upfront stress lead to the hypothesis that isolated sub-surface anticyclones are formed when a dipole that propagates away from a front is broken apart due to the upper cyclonic component being subject to an additional advection due to the Ekman flow. This hypothesis is investigated here across a range of parameters with a hierarchy of models.

a. Kinematic model

Manucharyan and Timmermans (2013) set out a simple kinematic model for dipole propagation in the absence of any effects other than the mutual interaction within the dipole. The model for the time evolution of the center positions of the vortices in their model is

$$\dot{\mathbf{r}}_1 = \frac{U_1}{\Delta}\mathbf{k} \times (\mathbf{r}_2 - \mathbf{r}_1), \tag{9a}$$

$$\dot{\mathbf{r}}_2 = \frac{U_2}{\Delta}\mathbf{k} \times (\mathbf{r}_2 - \mathbf{r}_1) \tag{9b}$$

where $\mathbf{r_1}$ is the position vector for the center of the cyclone, $\mathbf{r_2}$ is the position vector for the center of the anticyclone, $\mathbf{k}$ is the unit vertical vector, and a dot indicates the time derivative. We note again that Δ is the separation distance between the vortex centers, U_1 is the translation speed of the cyclone and U_2 is the translation speed of the anticyclone.

We modify this model to allow for an Ekman-induced flow that advects only the cyclone. This differential effect causes the separation distance Δ between the vortices to vary in time and we expect that increasing this distance reduces the rate that the dipole self-propagates at. Manucharyan and Timmermans (2013) show that if the dipole components are approximated as point vortices in a 2 1/2 layer model, the decay rate of the baroclinic modes is a modified Bessel function $K_0(r/\lambda)$, where in this case r is the radial distance from the centre of the cyclone and $\lambda \approx 4$ km is the mixed layer deformation radius. As such, we also multiply the first term by a factor that captures this decrease in self-propagation as the vortex separation increases:

$$\dot{\mathbf{r}}_1 = \frac{U_1}{\Delta(t)}\mathbf{k} \times (\mathbf{r}_2 - \mathbf{r}_1) \cdot K_0(\Delta(t)/\lambda) + A\mathbf{u}_{\mathrm{Ek}}, \tag{10a}$$

$$\dot{\mathbf{r}}_2 = \frac{U_2}{\Delta(t)}\mathbf{k} \times (\mathbf{r}_2 - \mathbf{r}_1) \cdot K_0(\Delta(t)/\lambda), \tag{10b}$$

where the Ekman velocity $\mathbf{u}_{\mathrm{Ek}} = (\mathbf{k} \times \tau)/(\rho f H_{\mathrm{Ek}})$ and the constant is inferred below to be $A = H_{\mathrm{Ek}}/H_{\mathrm{strat}}$. The applicability of this simple model is tested in Section 4e below.

b. Dynamic model

We derive a dynamical model for the effect of a surface stress acting on a geostrophic vortex in the mixed layer, following Stern (1965). The model provides a prediction for the velocity at which an isolated mixed layer vortex is translated due to the effects of a surface stress and this prediction is tested in Section 4e.

The domain for the dynamical model has an upper and a lower boundary. The upper boundary is where the effects of the surface stress are imposed. The lower boundary corresponds to the stratification at the base of the mixed layer of the MITgcm model. We assume that there are buoyancy anomalies at the upper boundary that can drive the flow in the interior but that there are no buoyancy anomalies at the lower boundary, as in the 'surface quasi-geostrophy' model of Lapeyre and Klein (2006), for example. The domain has no lateral boundaries.

The flow in the domain is assumed to be in geostrophic balance. The pressure field that balances this geostrophic flow is set by buoyancy anomalies at the upper boundary while potential vorticity anomalies in the interior of the domain are assumed to be zero. As a further simplification, we assume that the stratification $N^2 = \partial b/\partial z$ is constant in the layer.

A key assumption of the Stern (1965) model is that the Ekman layer is much thinner than the surface layer thickness. As such, the effect of convergences and divergences in the Ekman transport are parameterized as an ageostrophic vertical velocity at the upper boundary. In this case, the convergences and divergences in the Ekman transport occur due to lateral variations in the vertical component of relative vorticity (Stern 1965). In order to maintain a boundary condition of zero vertical velocity at the surface, the 'geostrophic' vertical velocity that can advect the buoyancy field is taken to be opposite and equal to the ageostrophic vertical velocity.

The model derivation set out in the Appendix shows that a surface stress is predicted to lead to the advection of anomalies in the domain of the dynamical model – where this domain corresponds to the mixed layer of the numerical simulations. The dynamical model has two limiting cases. For a given stratification there is a long wave limit where $NHl/f << 1$ and a short wave limit where $NHl/f >> 1$ where l is the wavenumber of the anomaly. For a given anomaly lengthscale the long wave limit can also be thought of as the weak stratification limit while the short wave limit can also be thought of as the strong stratification limit.

In the short wave limit the zonal phase velocity c of anomaly propagation is

$$c \propto -\frac{\tau^x}{\rho_0 f}\frac{Nl}{f}. \tag{11}$$

The short wave propagation is thus dispersive. On the other hand, in the long wave limit

$$c \propto -\frac{\tau^x}{\rho_0 f H_{\rm strat}} = u_{\rm Ek}\frac{H_{\rm Ek}}{H_{\rm strat}}. \tag{12}$$

We use $H_{\rm strat}$ as the vertical scale height. The mixed layer depth could also be used as the vertical scaling as the mixed layer depth scales linearly with $H_{\rm strat}$. In the long wave limit the anomalies propagate at a rate the scales with the Ekman transport divided by the scale height of the upper layer. For the Base experiment we find that $NHl/f \approx 0.2$ and so the model predicts that the surface cyclone should be advected at a rate that scales approximately with the long wave phase speed in equation (12). We test this prediction in the numerical simulations below.

c. Set-up of MITgcm Restart simulations

For these Restart experiments, a simulation with no surface stress is first run. The output of these simulations are examined to find a time point when a dipole has emerged from one of the fronts. This time point is then used as the initial condition for the Restart experiments. The vorticity distribution at the restart time for $H_{\rm strat} = 30$ m is shown in Fig. 8 (b).

Unlike the original experiment, a surface stress is applied to the Restart experiments. In each case the magnitude of the surface stress is increased linearly from zero to its final value over one day. In the Restart experiments the direction of the surface stress is set relative to the axis of the dipole i.e. the line connecting the center of the cyclone-anticyclone dipole pair.

The Restart experiments can be broken into two groups. In the first group of Restart experiments the surface stress is applied in each of the four cardinal directions relative to the dipole axis. The surface stress has a magnitude of 0.03 N m^{-2} in these experiments. For these experiments the original NoStress simulation at 250 m is used to generate the initial condition.

In the second group of Restart experiments a range of the stratification depths and surface stress magnitudes are used. For the simulations where $H_{\text{strat}} = 30$ m the original NoStress simulation is used to generate the initial condition, otherwise new simulations with no surface stress are used to generate the initial condition. In all of these experiments the surface stress is aligned so as to most efficiently breakup the dipole that is present in their intitial condition.

d. Simulations with varied surface stress directions

We restart the NoStress experiment on day 30 at the point when a self-propagating dipole has emerged from the front. This allows us to test the hypothesis that dipole breakup can occur rapidly due to the effect of a surface stress.

The surface stress is applied to four separate restarts of the NoStress experiment on day 30 with the surface stress applied in each case in one of the four cardinal directions relative to the axis separating the centers of the cyclone and anticyclone. The trajectories of the surface cyclone and sub-surface anticyclone in the following 15 days are shown in Fig. 8 based on model outputs at 0.5 day intervals.

As noted above in Section 3a, the dipole trajectory in the control case with no surface stress is an approximately circular path Fig. 8 a,b). This trajectory is consistent with Manucharyan and Timmermans (2013).

When the Ekman transport flows from the core of the anticyclone towards the core of the cyclone (red colors in Fig. 8 a,b), the dipole breaks apart within a few days as the surface cyclone travels southwest in the direction of the Ekman transport (Fig. 8 a) while the sub-surface anticyclone gradually loses speed and ceases to translate, as shown by the increasing clustering of the points marking the anticyclone location (Fig. 8 b). The trajectory of the cyclone is largely parallel to the direction of the Ekman transport, before its direction of travel begins to deviate as it is affected by a large cyclonic eddy to its southeast.

When the Ekman transport flows in the same direction as the dipole propagation (magenta colors in Fig. 8), the cyclone travels northwest in the same direction as the NoStress case, but on a straighter trajectory (Fig. 8a). The anticyclone also travels on a straighter trajectory in the first 10 days (Fig. 8b). Towards the end of the trajectory, the anticyclone does an orbit around the cyclone – as shown by the loop in (Fig. 8b) – at a much faster rate than occurs in the NoStress case.

When the Ekman transport flows in the opposite direction to the dipole propagation (blue colors in Fig. 8), the cyclone initially travels in the same direction as the NoStress case (Fig. 8a,b) though on a more curved path. As the cyclone follows this curved path (Fig. 8a) the angle of the dipole with respect to the Ekman transport changes such that the Ekman transport now develops a component flowing from the anticyclone towards the cyclone. This scenario again leads to the breakup of the dipole. The cyclone first translates away from the anticyclone along the axis connecting them (Fig. 8a) and then translates in the direction of the Ekman transport (Fig. 8a). Once the separation of the cyclone and anticyclone increases the anticyclone again gradually loses speed and ceases to translate (Fig. 8b).

Finally, when the Ekman transport flows from the cyclone towards the anticyclone (Fig. 8 a) (green colors in Fig. 8), the separation between the cyclone and anticyclone is reduced as the anticyclone initially follows the same path as in the NoStress experiment (Fig. 8 b). Again, the anticyclone does a fast loop of the cyclone (Fig. 8 b). An animated version of Fig. 8 showing this range of behavior can be found in the github repository (see Acknowledgments).

Overall, we see that where the Ekman flow has a component flowing in the direction that runs from the anticyclone to the cyclone it can detach the cyclone from the dipole. As dipoles follow a curved trajectory, this means that the dipole can move from an orientation that does not cause breakup of the dipole to an orientation that does cause breakup of the dipole with a surface stress in a fixed direction. Manucharyan and Timmermans (2013) find that cyclones tend to be stronger than anticyclones in dipoles and so the cyclone tends to be on the inside of the semi-circular trajectory i.e. on the side closest to the original front. This arrangement means that a surface stress that is upfront relative to the original front will have an Ekman flow suited to breaking apart dipole structures. Furthermore, this Ekman flow tends to carry the cyclonic component of the dipole back towards the original front, where it is re-entrained in the geostrophic turbulence associated with the front.

e. Simulations with varied surface stress magnitude and stratification depth

The kinematic model for the propagation of each component of the dipole in Section 10 is based on the hypothesis that in a steady state the velocity of the cyclone and anticyclone components of the dipole is a combination of the self-propagation due to the dipole and a velocity proportional to the Ekman velocity u_{Ek} that acts only on the cyclone.

In order to apply the kinematic model in equation (10), we need the scaling parameter A for the Ekman velocity. The dynamic model in Section 4b suggests that the scaling parameter is

$H_{\mathrm{Ek}}/H_{\mathrm{strat}}$. We can test this prediction for the scaling parameter by tracking the translation velocity of cyclones after the breakup of dipoles. To provide better support for this prediction we run experiments where the surface stress and the stratification depth are varied over a range of values. The surface stress is always oriented in these experiments in the direction that will breakup the dipole most efficiently i.e. with an Ekman transport that flows from the anticyclone towards the cyclone in their alignment at the restart point.

From this total group of experiments we then extract the cyclone translation velocity in the direction of the Ekman flow. In all cases the cyclone is influenced to some extent by other eddies in its vicinity. For the scaling comparison we omit experiments where the cyclone advection is clearly dominated by the influence of a nearby eddy. A comparison of the actual cyclone translation velocity with the proposed scaling velocity (Fig. 9) shows that the scaling $u_{\mathrm{cyc}} = (H_{\mathrm{Ek}}/H_{\mathrm{strat}})u_{\mathrm{Ek}}$ does capture the variation in cyclone translation over a wide range of surface stress magnitudes and stratification depths. The variance with respect to the scaling is primarily due to the effect of other eddies in the vicinity.

Using the scaling from the dynamical model in the kinematic model, we can test whether it captures the essential elements of the translation of the cyclone and anticyclone both before and after the breakup of the dipole. As the kinematic model is a steady state model, we increase the Ekman term linearly to its final value over the first two days to account for the time required for the steady Ekman flow to spin-up.

For a weaker surface stress (Fig. 10, a) the dipole maintains a trajectory that is similar to the NoStress simulation. The kinematic model over-predicts the extent to which the cyclone is advected away from the anticyclone in this case. As the surface stress increases (Fig. 10, b) the kinematic model captures the tendancy of the cyclone to translate in the direction of the Ekman flow and the deceleration of the anticyclone. As the surface stress increases further (Fig. 10, c), the

kinematic model correctly predicts a dipole breakup that occurs sooner than the previous experiment with the cyclone translating further in the Ekman direction and the anticyclone decelerating sooner. The translation speed of the anticyclone also decreases rapidly as the vortices become separated.

The kinematic model underpredicts the cyclone translation speed in the simulations with $H_{\text{strat}} = 30$ m (Fig. 9). This model underprediction is due to additional accelerations felt by the cyclone due to a low pressure region to its southeast (not shown).

5. Discussion

Numerical experiments presented here show that a surface stress in the opposite direction to the geostrophic flow helps cyclone-anticyclone dipoles to propagate away from surface fronts while a surface stress aligned with the geostrophic flow inhibits dipole propagation away from surface fronts. Furthermore, the numerical experiments show that when dipoles form and propagate away from the front the dipoles can be broken up by the Ekman transport induced by the surface stress, regardless of the surface stress applied at the time when the dipole was formed. The dipole breakup occurs when the mixed layer cyclonic component is advected by the Ekman flow away from the sub-surface anticyclonic component. Once the dipole has broken up the cyclonic vortex is advected primarily in the direction of the Ekman flow while the anticyclone comes to a halt. The orientation of dipoles is such that dipole breakup typically occurs when the surface stress has an upfront orientation relative to the original baroclinic front and so the cyclone is advected back towards the original front. These experiments are carried out under a range of parameters relevant to the Arctic Ocean.

Sensitivity experiments suggest that the formation of sub-surface anticyclones occurs once the Ekman flow is strong enough to advect the cyclone away from the anticyclone. However, for weak

initial lateral buoyancy gradients the eddy-driven processes tend to be dominated by Ekman-driven restratification and sub-surface eddies do not form.

There is no evidence from the numerical simulations that the sub-surface anticyclone is advected by the surface layer Ekman flow. This lack of anticyclone propagation is an interesting result. Morel and Thomas (2009) find in a shallow water model that anticyclones in the second layer are also advected due to surface stress effects. In Stern (1965) and in this paper the surface stress is parameterized as a vertical pumping at the upper boundary of the upper geostrophic layer. On the other hand, Morel and Thomas (2009) parameterize the surface stress as an advection throughout the upper layer. As such, the Ekman flow can advect thickness anomalies at the base of the upper layer in the Morel and Thomas (2009) approach and so the Ekman flow can advect sub-surface eddies. The primitive equation simulations in this paper suggest that the vertical pumping approach – that does not allow for Ekman advecection of thickness anomalies at the base of the upper layer – is preferable. The lack of sub-surface anticyclone translation due to surface stress effects means that a further mechanism is required to explain the presence of such sub-surface vortices a long distance from the surface fronts where they are thought to be formed (Timmermans et al. 2008). The most likely mechanism is advection by larger scale barotropic or deep baroclinic modes (Hogg and Stommel 1990).

The idea presented here – that dipoles can be broken apart by a vertical shear – is similar in some respects to the results of Chao and Shaw (1998), who considerd the case of a vertically-aligned dipole. However, Chao and Shaw (1998) attribute the dipole breakup to a process analogous to the Kutta-Zhukhovski lift theorem of potential flow around a solid rotating cylinder. In this analogy, a pressure differential arises across the cyclone due to the alignment of the rotation of the eddy and the Ekman flow on one side of the cyclone, but the opposition of the rotation of the eddy and the Ekman flow on the other side of the cyclone. However, such pressure differentials do not

arise for geophysical vortices as they do for solid cylinders, as the flow around the vortex balances the radial pressure gradients in a way that cannot occur for solid cylinders. We conclude that the evidence presented here shows that it is the differential Ekman advection in depth that leads to the breakup of the dipoles rather than any 'lift' effect.

The sub-surface anticyclones in these simulations are stable structures that persist throughout our simulations. There is little evidence in the simulations for the sub-surface anticyclones to grow through the merger of eddies. The lack of eddy mergers may reflect the 'halo' of cyclonic vorticity around the sub-surface anticyclones (Fig. 3, e). This positive potential vorticity anomaly can offset the negative potential vorticity anomaly in the core of the anticyclone. As such the far-field effect of the anticyclones is weakened and mergers of anticyclones is less common (Thomson and McIntyre 2016).

Idealized numerical experiments by Davis et al. (2014) and Manucharyan et al. (2016) indicate that eddy fluxes rather than vertical diffusion balance the Ekman transport that drives the Beaufort gyre. As such, the lifecycles of the observed eddies must be clarified in order to understand their role in the zeroth-order balance of the Arctic Ocean circulation. However, the eddies in the Davis et al. (2014) and Manucharyan et al. (2016) simulations are primarily first baroclinic mode structures that extend much deeper than the sub-surface eddies considered here. Reconciling the observed eddy field in the Arctic and the overall dynamical balance is a major outstanding question.

The results presented here may be of relevance for other regions of the ocean. A similar profile of vertical stratification is seen in the Bay of Bengal, for example, where there is also a shallow mixed layer overlying a strong halocline (MacKinnon et al. 2016). The northern Bay of Bengal experiences a sustained upfront stress each year as steady monsoon winds lead to the Ekman transport of fresher water from the western side of the bay over more saline water in the interior

of the bay. In a high resolution numerical simulation Sarkar et al. (2016) find that regions of anomalously low potential vorticity form underneath these fronts following baroclinic instability under an upfront surface stress. The formation of such low potential vorticity features could reflect the same process of dipole breakup set out here.

Finally, the results presented here suggest that although the sub-surface eddies may have a diameter of close to 10 kilometers, their formation may depend on baroclinic instability with a smaller lengthscale. As such, capturing the formation of sub-surface anticyclones in regional-scale simulations of the Arctic Ocean may be marginal even at a horizontal grid spacing of 1 km.

Acknowledgments. The python scripts used to generate the model input are available at `https://github.com/braaannigan/subsurface_eddy_generation_arctic_fronts_brannigan_et_al_2017`. along with an animated version of Fig. 8. The model version used was downloaded from mitgcm.org on 20th August 2015. The simulations are compiled with gfortran and run on the UK ARCHER supercomputer, a Cray XC30 system. LB, CL were funded by UK Natural Environment Research Council (NERC) TEA-COSI grant (The Environment of the Arctic: Climate, Ocean and Sea-Ice), HLJ was funded in part by the Overturning in the Subpolar North Atlantic project (OSNAP) while LB was also funded by Wenner-Grenn Stiftelsen. We thank two anonymous reviewers for their comments that helped to improve the manuscript.

APPENDIX A

Dynamical model for the advection of surface layer anomalies due to a surface stress

Building on the study of Stern (1965), we present a linearised model of how interactions between surface Ekman and geostrophic flows cause propagation of the geostrophically-balanced flow component. The model describes a weakly stratified surface layer with constant buoyancy frequency,

having a large buoyancy jump at its base. The buoyancy jump is large enough that the base of the surface layer acts a rigid flat bottom. The sea surface also acts as rigid lid. The pressure and buoyancy fields are related via hydrostatic balance

$$\frac{\partial \phi}{\partial z} = b. \tag{A1}$$

where ϕ is the dynamic pressure. The interior velocity field is in geostrophic balance, implying that $\psi \equiv \phi / f$ is a streamfunction for the horizontal flow in the interior. The linearised buoyancy equation for the interior flow is

$$\frac{\partial b}{\partial t} + wN^2 = 0, \tag{A2}$$

where horizontal buoyancy advection due the geostrophic flow has been neglected.

For the lower boundary condition at $z = -H_{\text{strat}}$ we assume that there are no buoyancy anomalies and no vertical velocities and so $b = 0$ and $w = 0$. For the upper boundary condition at $z = 0$ we use the approach of Stern (1965) whereby the sum of the geostrophic and Ekman vertical velocities is zero at the upper boundary: $w + w_{\text{Ek}} = 0$. Thus equation (A2) at the upper boundary becomes:

$$\frac{\partial b}{\partial t} - w_{\text{Ek}} N^2 = 0. \tag{A3}$$

where the Ekman vertical velocity from Stern (1965) is

$$w_{\text{Ek}} = \frac{\tau^x}{\rho_0 f^2} \frac{\partial \zeta}{\partial y} \tag{A4}$$

for a constant surface stress τ^x taken to be in the zonal direction.

In the interior the potential vorticity q vanishes and so

$$q = \nabla_h^2 \phi + \frac{f^2}{N^2} \frac{\partial^2 \phi}{\partial z^2} = 0 \tag{A5}$$

where ϕ is the dynamic pressure and we assume that N^2 is constant. In hydrostatic balance we can also rewrite equation (A3) for the advection of anomalies on the upper boundary in terms of ϕ as

$$\frac{\partial^2 \phi}{\partial z \partial t} - \frac{\tau^x}{\rho_0 f^3} \frac{\partial^3 \phi}{\partial y^3} N^2 = 0. \tag{A6}$$

In equation (A6) we use (A4) to replace the Ekman vertical velocity in the second term and the relation $\zeta = \phi_{yy}/f$.

Before finding solutions to equation (A6) we use equation (A5) to establish the vertical structure. We assume that perturbations have a wave-like structure in the meridional direction with $\phi = \Phi(z)e^{i\omega t - ily}$ and so equation (A5) becomes

$$\frac{d^2\Phi}{dz^2} - \frac{l^2N^2}{f^2}\Phi = 0. \tag{A7}$$

The solution for Φ is thus

$$\Phi = C_1 \cosh(\frac{lN}{f}z) + C_2 \sinh(\frac{lN}{f}z) \tag{A8}$$

where C_1 and C_2 are constants. At the lower boundary where $z = -H_{\text{strat}}$ there are no buoyancy anomalies and so $b = \Phi_z = 0$. Differentiating equation (A8) with respect to z and evaluating it at $z = -H_{\text{strat}}$ gives

$$-C_1 \sinh(\frac{lNH_{\text{strat}}}{f}) + C_2 \cosh(\frac{lNH_{\text{strat}}}{f}) = 0 \tag{A9}$$

or

$$C_2 = C_1 \tanh(\frac{lNH_{\text{strat}}}{f}) \tag{A10}$$

and so we look for solutions of the form

$$\phi \propto e^{i\omega t - ilx}\left[\cosh\left(\frac{Nl}{f}z\right) + \tanh\left(\frac{NlH_{\text{strat}}}{f}\right)\sinh\left(\frac{Nl}{f}z\right)\right]. \tag{A11}$$

Inserting equation (A11) at the upper boundary where $z = 0$ into equation (A6), we obtain the dispersion relation

$$\omega = -\frac{l^2N\tau^x}{\rho_0 f^2}\frac{1}{\tanh(lNH_{\text{strat}}/f)}. \tag{A12}$$

For the phase speed ($c = \omega/l$) there is a long wave limit ($NH_{\text{strat}}l/f \ll 1$):

$$c \propto -\frac{\tau^x}{\rho_0 f H_{\text{strat}}}, \tag{A13}$$

that is the Ekman transport divided by the depth of the upper layer. Alternatively, this can be thought of as $c \propto u_{\mathrm{Ek}}(H_{\mathrm{Ek}}/H_{\mathrm{strat}})$. The results in Section 4e suggest that the scaling coefficient for the phase speed is approximately 1 in the longwave case. The relation found in equation (A13) is analogous to the corresponding limit in Stern's two layer case (where $H = H_1 + H_2$).

In the short wave limit, the phase velocity is

$$c \propto -\frac{\tau^x}{f}\frac{Nl}{f}, \tag{A14}$$

showing that short disturbances have phase velocities that increase with wave number.

References

Alkire, M. B., K. K. Falkner, I. Rigor, M. Steele, and J. Morison, 2007: The return of Pacific waters to the upper layers of the central Arctic Ocean . *Deep Sea Research Part I: Oceanographic Research Papers*, **54 (9)**, 1509 – 1529, doi:http://dx.doi.org/10.1016/j.dsr.2007.06.004.

Brannigan, L., 2016: Intense submesoscale upwelling in anticyclonic eddies. *Geophysical Research Letters*, **43 (7)**, 3360–3369, doi:10.1002/2016GL067926.

Brannigan, L., D. P. Marshall, A. Naveira-Garabato, and G. A. Nurser, 2015: The seasonal cycle of submesoscale flows. *Ocean Modelling*, **92 (0)**, 69–84.

Buckingham, C. E., and Coauthors, 2016: Seasonality of submesoscale flows in the ocean surface boundary layer. *Geophysical Research Letters*, **43 (5)**, 2118–2126, doi:10.1002/2016GL068009.

Chao, S.-Y., and P.-T. Shaw, 1996: Initialization, asymmetry, and spindown of arctic eddies. *Journal of Physical Oceanography*, **26 (10)**, 2076–2092, doi:10.1175/1520-0485(1996)026⟨2076:IAASOA⟩2.0.CO;2, URL https://doi.org/10.1175/1520-0485(1996)026⟨2076:IAASOA⟩2.0.CO;2, https://doi.org/10.1175/1520-0485(1996)026⟨2076:IAASOA⟩2.0.CO;2.

Chao, S.-Y., and P.-T. Shaw, 1998: Eddy Maintenance and Attrition in a Vertically Sheared Current under Arctic Ice. *Journal of Physical Oceanography*, **28 (12)**, 2427–2443, doi: 10.1175/1520-0485.

Cole, S. T., M.-L. Timmermans, J. M. Toole, R. A. Krishfield, and F. T. Thwaites, 2014: Ekman Veering, Internal Waves, and Turbulence Observed under Arctic Sea Ice. *Journal of Physical Oceanography*, **44 (5)**, 1306–1328, doi:10.1175/JPO-D-12-0191.1.

Daru, V., and C. Tenaud, 2004: High order one-step monotonicity-preserving schemes for unsteady compressible flow calculations. *Journal of Computational Physics*, **193 (2)**, 563–594.

D'Asaro, E. A., 1988: Observations of small eddies in the Beaufort Sea. *J. Geophys. Res.*, **93 (C6)**, 6669–6684, URL http://dx.doi.org/10.1029/JC093iC06p06669.

Davis, P. E. D., C. Lique, and H. L. Johnson, 2014: On the Link between Arctic Sea Ice Decline and the Freshwater Content of the Beaufort Gyre: Insights from a Simple Process Model. *Journal of Climate*, **27 (21)**, 8170–8184, doi:10.1175/JCLI-D-14-00090.1.

Ekman, V. W., 1905: On the influence of the Earth's rotation on ocean currentsgu. *Ark.Mat.Astron.Fys.*, **2**, 1–53.

Fox-Kemper, B., R. Ferrari, and R. Hallberg, 2008: Parameterization of Mixed Layer Eddies. Part I: Theory and Diagnosis. *Journal of Physical Oceanography*, **38 (6)**, 1145–1165, doi:10.1175/2007JPO3792.1.

Graham, J. P., and T. Ringler, 2013: A framework for the evaluation of turbulence closures used in mesoscale ocean large-eddy simulations. *Ocean Modelling*, **65**, 25–39.

Griffies, S. M., and R. W. Hallberg, 2000: Biharmonic friction with a Smagorinsky-like viscosity for use in large-scale eddy-permitting ocean models. *Monthly Weather Review*, **128 (8)**, 2935–2946.

Hogg, N. G., and H. M. Stommel, 1985: The Heton, an Elementary Interaction Between Discrete Baroclinic Geostrophic Vortices, and Its Implications Concerning Eddy Heat-Flow. *Proceedings of the Royal Society A: Mathematical, Physical and Engineering Sciences*, **397 (1812)**, 1–20, doi:10.1098/rspa.1985.0001, URL http://rspa.royalsocietypublishing.org/cgi/doi/10.1098/rspa.1985.0001.

Hogg, N. G., and H. M. Stommel, 1990: How currents in the upper thermocline could advect meddies deeper down. *Deep Sea Research Part A. Oceanographic Research Papers*, **37 (4)**, 613–623, URL http://www.sciencedirect.com/science/article/pii/019801499090093B.

Hunkins, K. L., 1974: Subsurface eddies in the Arctic ocean. *Deep Sea Research and Oceanographic Abstracts*, **21 (12)**, 1017 – 1033, doi:http://dx.doi.org/10.1016/0011-7471(74)90064-3.

Ilicak, M., A. J. Adcroft, S. M. Griffies, and R. W. Hallberg, 2012: Spurious dianeutral mixing and the role of momentum closure. *Ocean Modelling*, **45-46**, 37–58.

Krishfield, R., J. Toole, A. Proshutinsky, and M. L. Timmermans, 2008: Automated ice-tethered profilers for seawater observations under pack ice in all seasons. *Journal of Atmospheric and Oceanic Technology*, **25 (11)**, 2091–2105, doi:10.1175/2008JTECHO587.1.

Lapeyre, G., and P. Klein, 2006: Dynamics of the upper oceanic layers in terms of surface quasi-geostrophy theory. *J.Phys.Oceanogr.*, **36 (2)**, 165–176.

Large, W. G., J. C. McWilliams, and S. C. Doney, 1994: Oceanic Vertical Mixing - a Review and a Model with a Nonlocal Boundary-Layer Parameterization. *Reviews of Geophysics*, **32 (4)**, 363–403.

MacKinnon, J. A., and Coauthors, 2016: A tale of two spicy seas. **29**, doi:10.5670/oceanog.2016.38.

Mahadevan, A., A. Tandon, and R. Ferrari, 2010: Rapid changes in mixed layer stratification driven by submesoscale instabilities and winds. *Journal of Geophysical Research-Oceans*, **115**, C03 017.

Manley, T. O., and K. Hunkins, 1985: Mesoscale eddies of the Arctic Ocean. *Journal of Geophysical Research: Oceans*, **90 (C3)**, 4911–4930, doi:10.1029/JC090iC03p04911.

Manucharyan, G. E., M. A. Spall, and A. F. Thompson, 2016: A Theory of the Wind-Driven Beaufort Gyre Variability. *Journal of Physical Oceanography*, **46 (11)**, 3263–3278, doi:10.1175/JPO-D-16-0091.1, http://dx.doi.org/10.1175/JPO-D-16-0091.1.

Manucharyan, G. E., and M.-L. Timmermans, 2013: Generation and separation of mesoscale eddies from surface ocean fronts. *Journal of Physical Oceanography*, **43 (12)**, 2545–2562.

Marshall, J., A. Adcroft, C. Hill, L. Perelman, and C. Heisey, 1997: A finite-volume, incompressible Navier Stokes model for studies of the ocean on parallel computers. *Journal of Geophysical Research-Oceans*, **102 (C3)**, 5753–5766.

Martin, T., M. Steele, and J. Zhang, 2014: Seasonality and long-term trend of Arctic Ocean surface stress in a model. *Journal of Geophysical Research: Oceans*, **119 (3)**, 1723–1738, doi:10.1002/2013JC009425, URL http://dx.doi.org/10.1002/2013JC009425.

718 Morel, Y., and L. N. Thomas, 2009: Ekman drift and vortical structures. *Ocean Modelling*, **27 (34)**,
719 185 – 197, doi:http://dx.doi.org/10.1016/j.ocemod.2009.01.002.

720 Newton, J., K. Aagaard, and L. Coachman, 1974: Baroclinic eddies in the Arctic Ocean. *Deep Sea*
721 *Research and Oceanographic Abstracts*, **21 (9)**, 707–719.

722 Padman, L., M. Levine, T. Dillon, J. Morison, and R. Pinkel, 1990: Hydrography and mi-
723 crostructure of an arctic cyclonic eddy. *J. Geophys. Res.*, **95 (C6)**, 9411–9420, doi:10.1029/
724 JC095iC06p09411.

725 Pedregosa, F., and Coauthors, 2011: Scikit-learn: Machine learning in Python. *Journal of Machine*
726 *Learning Research*, **12**, 2825–2830.

727 Pickart, R. S., T. J. Weingartner, L. J. Pratt, S. Zimmermann, and D. J. Torres, 2005: Flow of
728 winter-transformed Pacific water into the Western Arctic . *Deep Sea Research Part II: Topical*
729 *Studies in Oceanography*, **52 (2426)**, 3175 – 3198, doi:10.1016/j.dsr2.2005.10.009.

730 Plueddemann, A. J., R. Krishfield, T. Takizawa, K. Hatakeyama, and S. Honjo, 1998: Upper ocean
731 velocities in the Beaufort Gyre. *Geophys. Res. Lett.*, **25 (2)**, 183–186, doi:10.1029/97GL53638.

732 Ramachandran, S., A. Tandon, and A. Mahadevan, 2013: Effect of subgrid-scale mixing on the
733 evolution of forced submesoscale instabilities. *Ocean Modelling*, **66**, 45–63.

734 Sarkar, S., H. T. Pham, S. Ramachandran, J. D. Nash, A. Tandon, J. Buckley, A. A. Lotliker, and
735 M. M. Omand, 2016: The interplay between submesoscale instabilities and turbulence in the
736 surface layer of the Bay of Bengal. *Oceanography*, **29 (2)**, 146–157.

737 Smagorinsky, J., 1963: General circulation experiments with the primitive equations: I. The basic
738 experiment. *Mon.Weather Rev.*, **91 (3)**, 99–164.

739 Spall, M. A., 1995: Frontogenesis, subduction, and cross-front exchange at upper ocean fronts.
740 *Journal of Geophysical Research: Oceans (19782012)*, **100 (C2)**, 2543–2557.

741 Steele, M., J. Morison, W. Ermold, I. Rigor, M. Ortmeyer, and K. Shimada, 2004: Circulation of
742 summer Pacific halocline water in the Arctic Ocean. *J. Geophys. Res.*, **109 (C2)**, doi:10.1029/
743 2003JC002009.

744 Stern, M. E., 1965: Interaction of a uniform wind stress with a geostrophic vortex. *Deep Sea*
745 *Research and Oceanographic Abstracts*, Elsevier, Vol. 12, 355–367.

746 Stone, P. H., 1966: On Non-Geostrophic Baroclinic Stability. *Journal of the Atmospheric Sciences*,
747 **23 (4)**, 390–400.

748 Taylor, J. R., and R. Ferrari, 2010: Buoyancy and Wind-Driven Convection at Mixed Layer Den-
749 sity Fronts. *Journal of Physical Oceanography*, **40 (6)**, 1222–1242, doi:10.1175/2010JPO4365.
750 1.

751 Thomas, L., and R. Ferrari, 2008: Friction, Frontogenesis, and the Stratification of the Sur-
752 face Mixed Layer. *Journal of Physical Oceanography*, **38 (11)**, 2501–2518, doi:10.1175/
753 2008JPO3797.1, URL http://journals.ametsoc.org/doi/abs/10.1175/2008JPO3797.1.

754 Thomas, L. N., 2005: Destruction of potential vorticity by winds. *Journal of Physical Oceanog-*
755 *raphy*, **35 (12)**, 2457–2466.

756 Thomas, L. N., 2008: Formation of intrathermocline eddies at ocean fronts by wind-driven de-
757 struction of potential vorticity. *Dyn.Atmos.Oceans*, **45 (3)**, 252–273.

758 Thomas, L. N., and C. M. Lee, 2005: Intensification of ocean fronts by down-front winds. *Journal*
759 *of Physical Oceanography*, **35 (6)**, 1086–1102.

Thomas, L. N., and P. B. Rhines, 2002: Nonlinear stratified spin-up. *Journal of Fluid Mechanics*, **473**, 211–244, doi:10.1017/S0022112002002367.

Thomas, L. N., J. R. Taylor, R. Ferrari, and T. M. Joyce, 2013: Symmetric instability in the Gulf Stream. *Deep Sea Research Part II: Topical Studies in Oceanography*, **91**, 96–110, doi:10.1016/j.dsr2.2013.02.025.

Thompson, A. F., A. Lazar, C. Buckingham, A. C. N. Garabato, G. M. Damerell, and K. J. Heywood, 2016: Open-Ocean Submesoscale Motions: A Full Seasonal Cycle of Mixed Layer Instabilities from Gliders. *Journal of Physical Oceanography*, **46 (4)**, 1285–1307, doi:10.1175/JPO-D-15-0170.1, http://dx.doi.org/10.1175/JPO-D-15-0170.1.

Thomson, S. I., and M. E. McIntyre, 2016: Jupiters Unearthly Jets: A New Turbulent Model Exhibiting Statistical Steadiness without Large-Scale Dissipation. *Journal of the Atmospheric Sciences*, **73 (3)**, 1119–1141, doi:10.1175/JAS-D-14-0370.1, https://doi.org/10.1175/JAS-D-14-0370.1.

Timmermans, M.-L., S. Cole, and J. Toole, 2012: Horizontal Density Structure and Restratification of the Arctic Ocean Surface Layer. *Journal of Physical Oceanography*, **42 (4)**, 659–668, doi:10.1175/JPO-D-11-0125.1, http://dx.doi.org/10.1175/JPO-D-11-0125.1.

Timmermans, M.-L., J. Toole, A. Proshutinsky, R. Krishfield, and A. Plueddemann, 2008: Eddies in the Canada Basin, Arctic Ocean, Observed from Ice-Tethered Profilers. *Journal of Physical Oceanography*, **38 (1)**, 133–145, doi:10.1175/2007JPO3782.1, http://dx.doi.org/10.1175/2007JPO3782.1.

Toole, J., R. A. Krishfield, M.-L. Timmermans, and A. Proshutinsky, 2011: The ice-tethered profiler: Argo of the Arctic. *Oceanography*, **24 (3)**, 126–135, doi:10.5670/oceanog.2011.64.

Wenegrat, J. O., and M. J. McPhaden, 2016: Wind, Waves, and Fronts: Frictional Effects in a Generalized Ekman Model. *Journal of Physical Oceanography*, **46 (2)**, 371–394, doi:10.1175/JPO-D-15-0162.1, http://dx.doi.org/10.1175/JPO-D-15-0162.1.

Zhao, M., and M.-L. Timmermans, 2015: Vertical scales and dynamics of eddies in the Arctic Ocean's Canada Basin. *J. Geophys. Res. Oceans*, **120 (12)**, 8195–8209, doi:10.1002/2015JC011251.

Zhao, M., M.-L. Timmermans, S. Cole, R. Krishfield, A. Proshutinsky, and J. Toole, 2014: Characterizing the eddy field in the Arctic Ocean halocline. *Journal of Geophysical Research: Oceans*, **119 (12)**, 8800–8817, doi:10.1002/2014JC010488.

Zhao, M., M.-L. Timmermans, S. Cole, R. Krishfield, and J. Toole, 2016: Evolution of the eddy field in the Arctic Ocean's Canada Basin, 20052015. *Geophysical Research Letters*, **43 (15)**, 8106–8114, doi:10.1002/2016GL069671, 2016GL069671.

LIST OF TABLES

TABLE 1. Names and parameters used for the numerical experiments. τ_x is the zonal surface stress, $\mathbf{H}_{\text{strat}}$ is the stratification depth, **dSh** is the cross-front salinity difference, **r** estimates the relative role of Ekman to eddy-driven restratification and Ri is the balanced Richardson number.

Exp. name	$\triangle$**x**	τ_x	$\mathbf{H}_{\text{strat}}$	**dSh**	**r**	**Ri**
	(km)	10^{-2} N m^{-2}	(m)	psu	eqn. (6)	eqn. (7)
Base	0.25	3	30	1.25	1.3	1.8
NoStress	0.25	0	30	1.25	0.0	1.8
Base1000	1.0	3	30	1.25	1.3	1.8
Base0500	0.5	3	30	1.25	1.3	1.8
HalfStress	0.5	1.5	30	1.25	0.7	1.8
DoubleStress	0.5	6	30	1.25	2.6	1.8
H_{strat}20	0.5	3	20	1.25	3.0	2.7
H_{strat}40	0.5	3	40	1.25	0.8	1.7
dSH1.0	0.5	3	30	1	1.7	2.3
dSh0.75	0.5	3	30	0.75	2.4	3.0
dSh0.5	0.5	3	30	0.5	3.4	4.5
RestartH_{strat}30	0.5	0.00-0.06	30	1.25	0.0	1.8
RestartH_{strat}40	0.5	0.00-0.18	40	1.25	0.0-5.0	1.8
RestartH_{strat}60	0.5	0.00-0.40	60	1.25	0.0-2.4	1.8

LIST OF FIGURES

centres and the color arrows indicate the direction of the corresponding Ekman transport. Dots are shown at 0.5 day intervals. In (b) the normalized ζ^z/f field at 25 m depth is also shown in with a color range of -1 to 1. An animated version of this figure can be found in the github repository (see Acknowledgments). 50

Fig. 9. Comparison of the cyclone translation velocity in the direction of the Ekman flow (y-axis) with the prediction of the dynamic model (x-axis). Colors show the stratification depth for the experiment. The dashed black line is the line $y = x$. 51

Fig. 10. Trajectories of the surface cyclone (red dots) and sub-surface anticyclone (blue dots) with various surface stress directions in the 15 days after the surface stress is applied in RestartH_{strat}30 experiments. Eddy positions predicted by the kinematic model in equation (10) are shown as circles. The black arrow shows the direction of the surface stress and the green arrow shows the direction of the Ekman flow. Dots are shown at 0.5 day intervals. . . 52

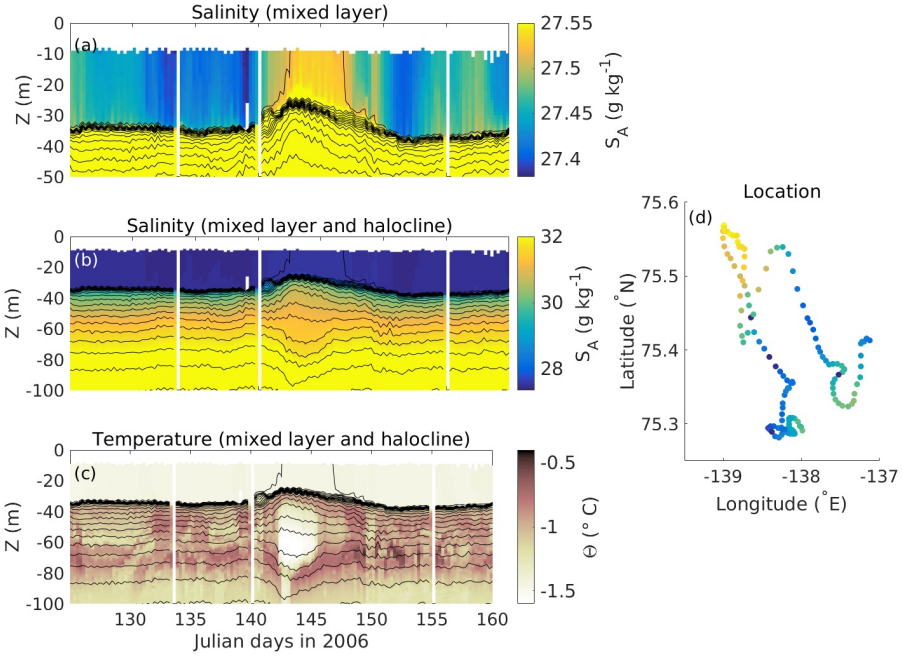

FIG. 1. An anticyclonic eddy observed below the base of the mixed layer in the Canada Basin by ITP3 in May 2006. (a) Absolute Salinity in the mixed layer. (b) Absolute salinity in the mixed layer and halocline. (c) Conservative temperature in the mixed layer and halocline. Black lines are contours of potential density with a contour interval of 0.2 kg m^{-3}. (d) Location of samples. Colors in (d) show salinity at $z = -15$ m with the same colormap as (a). The Ice-Tethered Profiler data were collected and made available by the Ice-Tethered Profiler Program (Krishfield et al. 2008; Toole et al. 2011) based at the Woods Hole Oceanographic Institution (http://www.whoi.edu/itp).

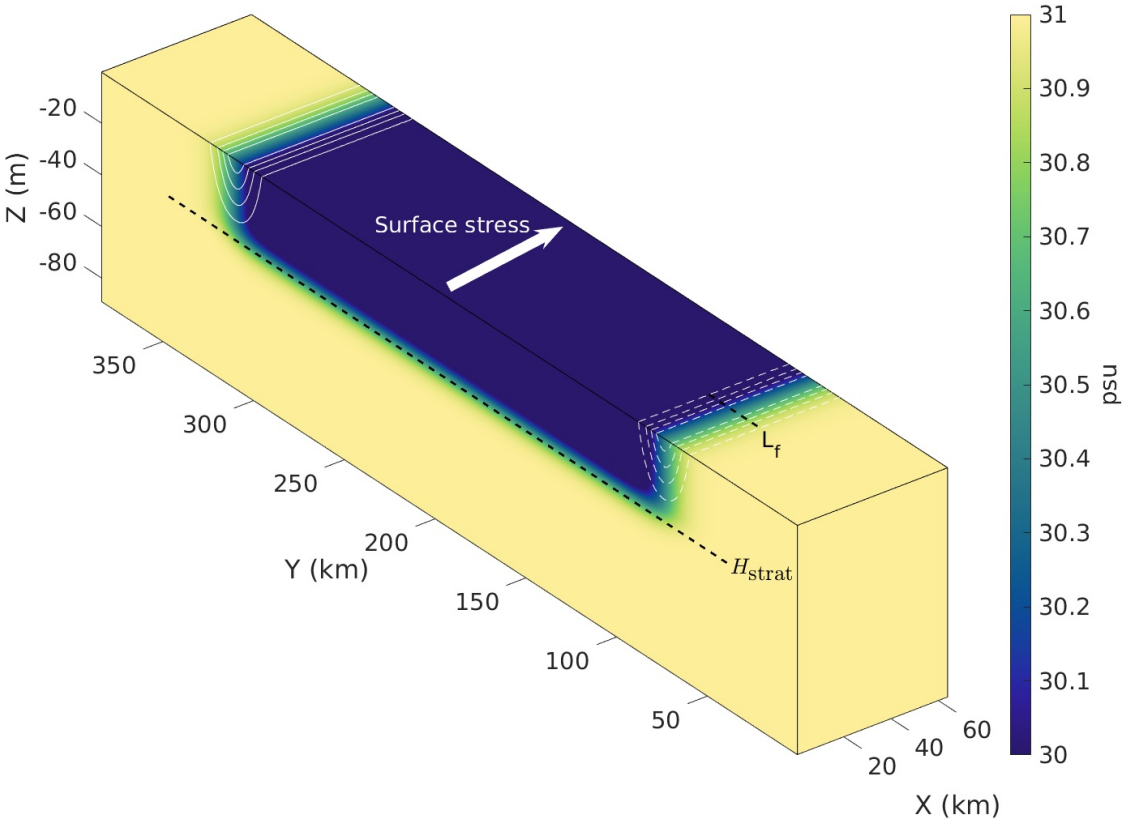

FIG. 2. The model domain and initial condition. The colors show the initial salinity distribution while the contour lines show the initial zonal velocity. The arrow shows the direction of the surface stress vector for the Base experiments. The contour interval is 0.02 m s^{-1} with solid contours for positive values and dashed contours for negative values.

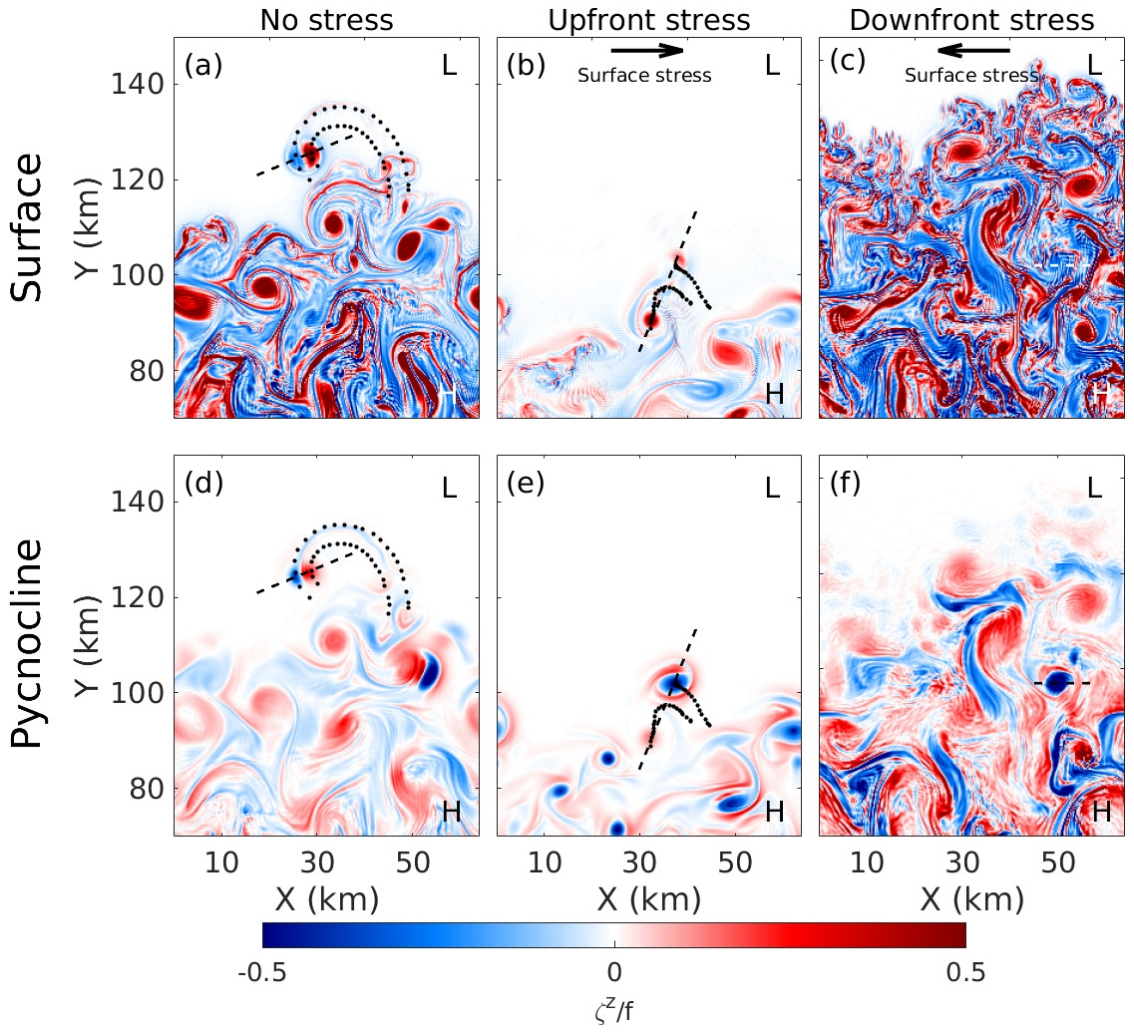

FIG. 3. Comparison of the vertical component of relative vorticity ζ normalized by f on day 44 for the experiments NoStress (left panels) and Base with $\tau_x = 0.03$ N m^{-2} (center and right panels). Black dots show the trajectories of the cyclone and anticyclone over days 26 to 46. The light (L) and heavy (H) side of the front is indicated on each plot. The orientation of the northern front in the right panels is reversed to allow comparisons. The arrow indicates the direction of the surface stress. The upper panels show values at the surface while the lower panels show values in the high stratification pycnocline at 34 m depth below the base of the mixed layer. Color values are saturated for the upper left-hand panel with local values greater than 1. The black horizontal lines show where the sections in Fig. 4 are taken.

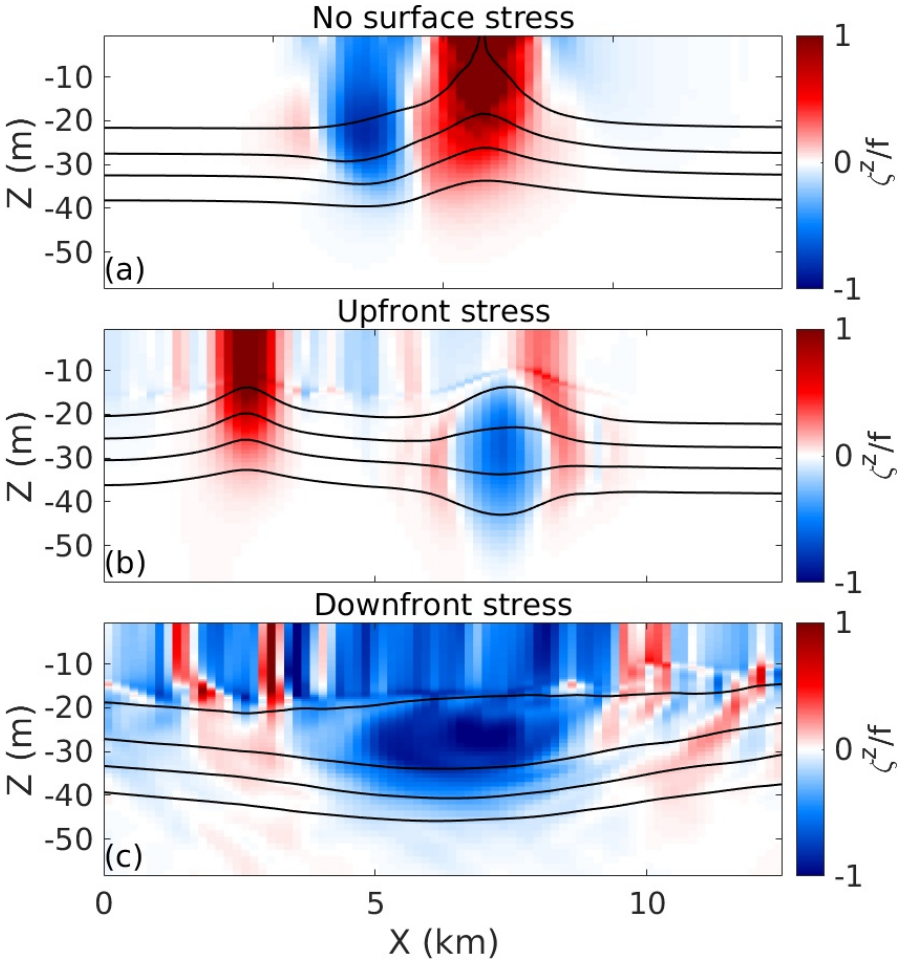

878 FIG. 4. Comparison of the vertical component of relative vorticity normalized by f on day 44 for the exper-
879 iments NoStress (a) and Base (b and c) with $\tau_x = 0.03$ N m^{-2}. Sections are taken along the black lines in Fig.
880 3. The black lines are isohalines with a contour interval of 0.25 psu. The color scale is saturated for positive
881 values.

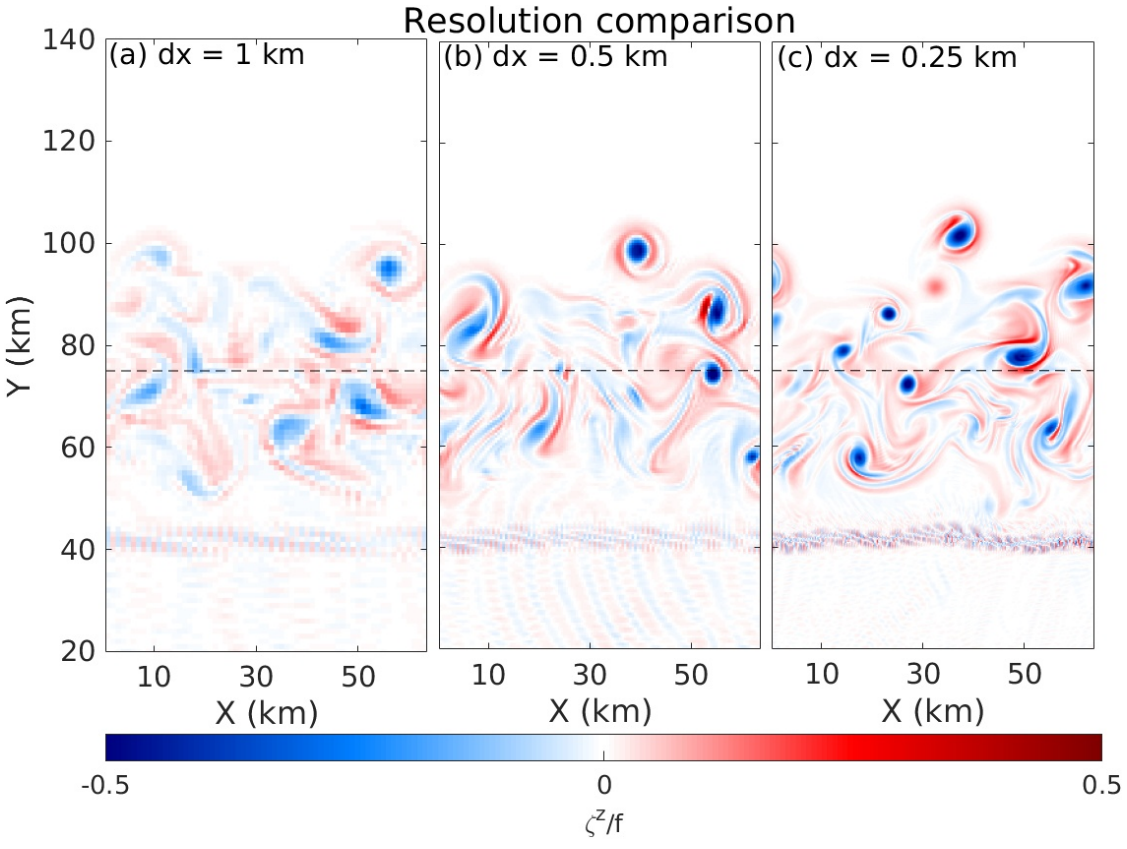

882 FIG. 5. Normalized relative vorticity at 34 m depth below the base of the mixed layer on day 42 with varying
883 grid resolution and an upfront surface stress. (a) Base1000 with 1 km resolution, (b) Base0500 with 0.5 km
884 resolution and (c) Base with 0.25 km resolution. The dashed lines show the position of the original front. The
885 color scale is saturated.

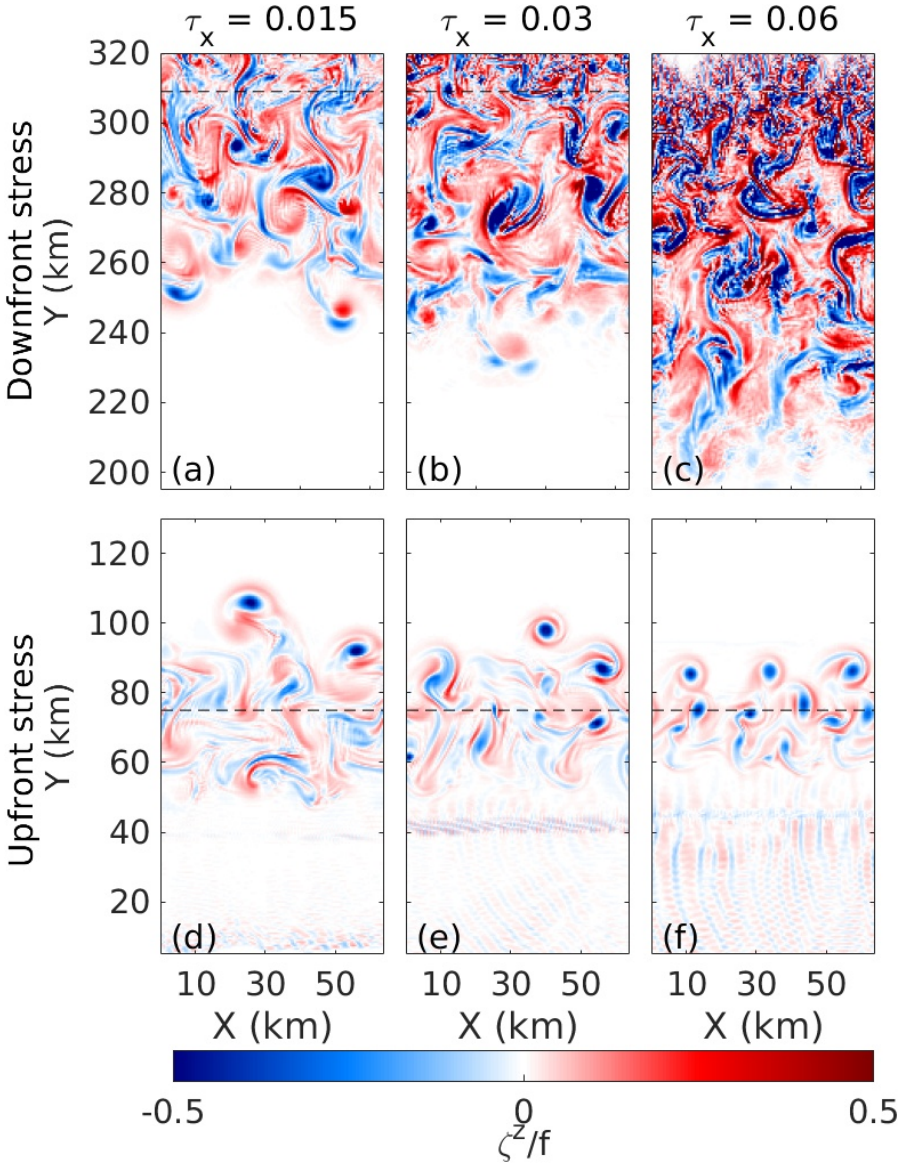

886 FIG. 6. Normalized relative vorticity at 34 m depth below the base of the mixed layer on day 39 at 0.5 km res-
887 olution with varying surface stress. Upper panels show the front with a downfront stress while the lower panels
888 show the front with an upfront stress with a gap in the y-axis between the upper and lower row. (a,d) HalfStress
889 with $\tau_x = 0.015$ N m^{-2}, (b,e) Base0500 with $\tau_x = 0.03$ N m^{-2} and (c,f) DoubleStress with $\tau_x = 0.06$ N m^{-2}.
890 The dashed lines show the position of the original front. The color scale is saturated.

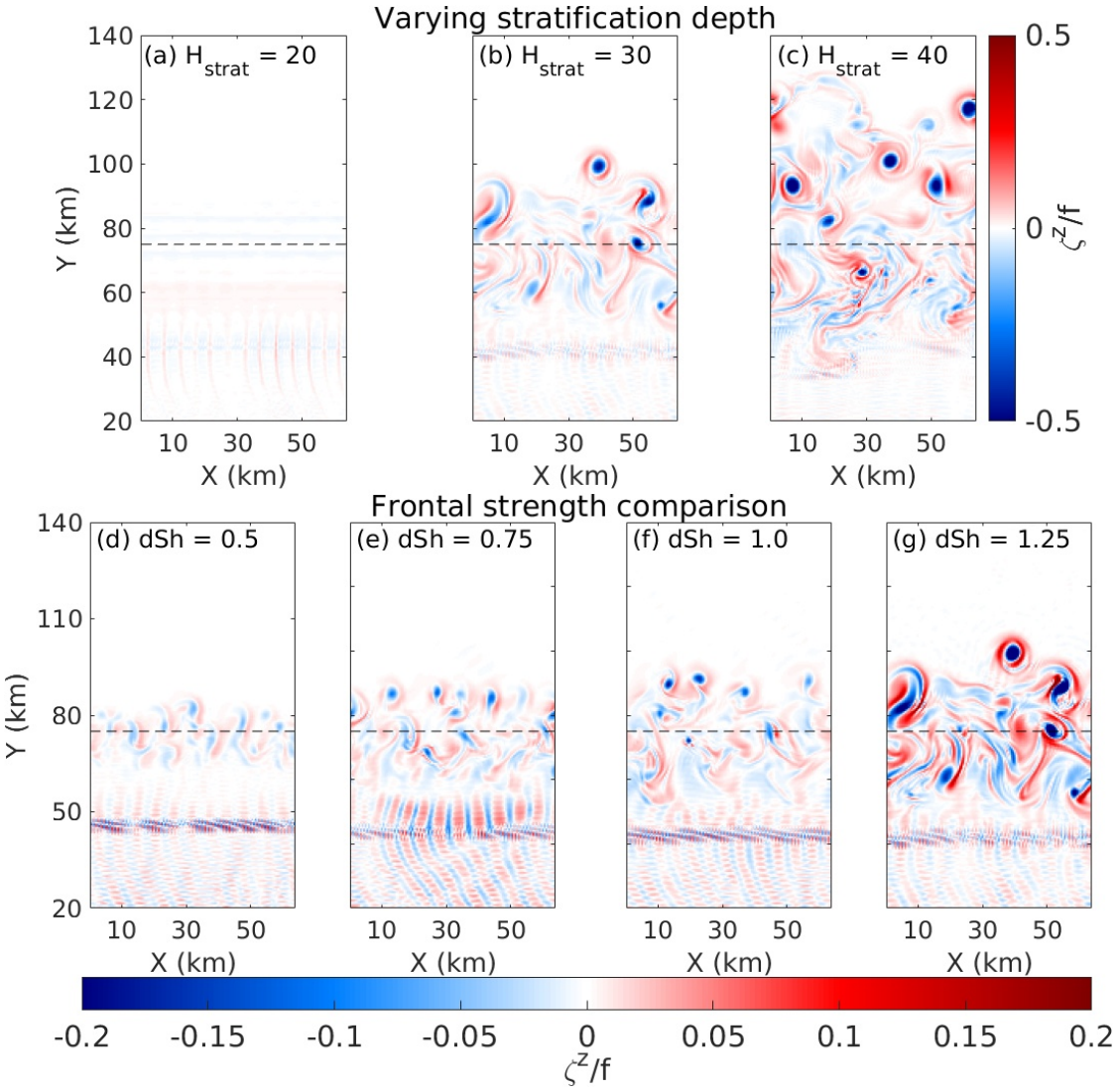

FIG. 7. Normalized relative vorticity at 34 m depth on day 45 at 0.5 km resolution with varying initial conditions and an upfront surface stress. (Upper row) Varying initial stratification depth. The plan view is at a depth of 15 m in (a), 30 m in (b) and 43 m in (c). (Lower row) Varying initial cross-front salinity. The dashed lines show the position of the original front. A smaller color range is used in the lower plots to allow the results for weaker fronts to be seen. The color scale is saturated.

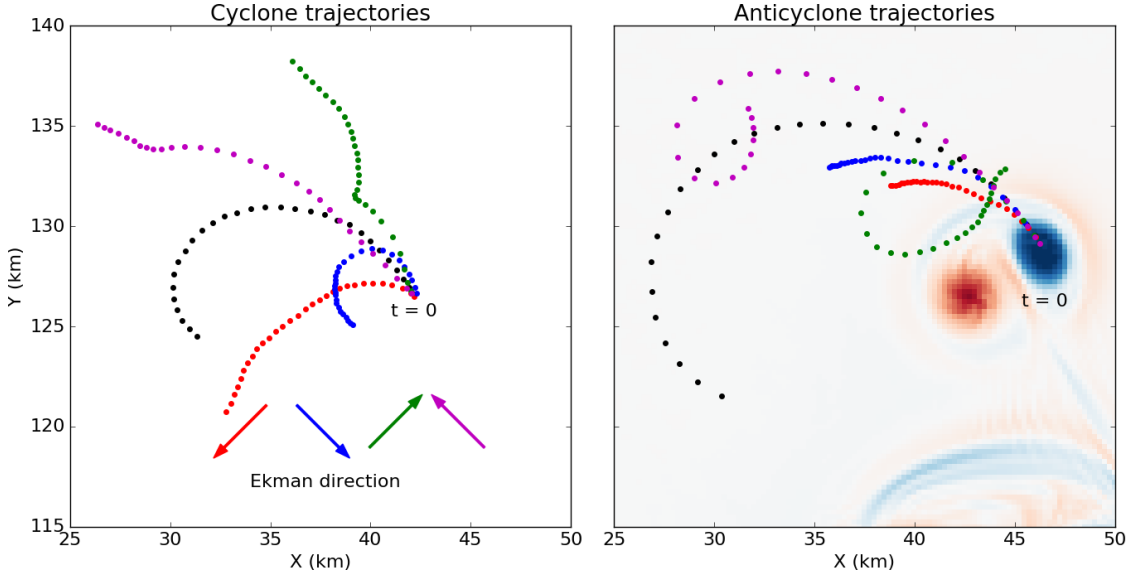

FIG. 8. Trajectories of the surface cyclone (a) and sub-surface anticyclone (b) in the 15 days after the surface stress is applied to the NoStress experiment. The black line shows the trajectories from the original NoStress experiment. The color dots show the trajectory for the vortex centres and the color arrows indicate the direction of the corresponding Ekman transport. Dots are shown at 0.5 day intervals. In (b) the normalized ζ^z/f field at 25 m depth is also shown in with a color range of -1 to 1. An animated version of this figure can be found in the github repository (see Acknowledgments).

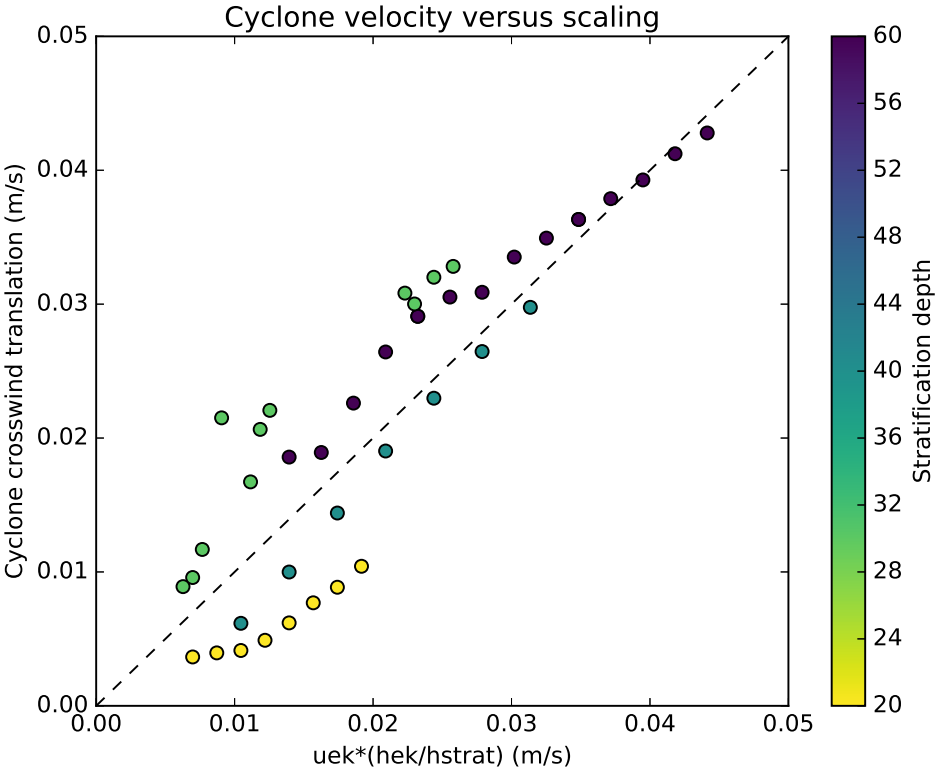

902 FIG. 9. Comparison of the cyclone translation velocity in the direction of the Ekman flow (y-axis) with the
903 prediction of the dynamic model (x-axis). Colors show the stratification depth for the experiment. The dashed
904 black line is the line $y = x$.

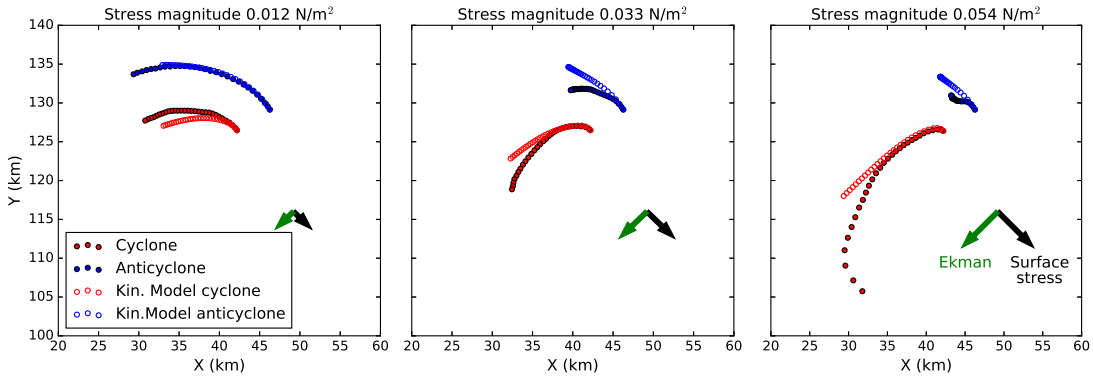

905 FIG. 10. Trajectories of the surface cyclone (red dots) and sub-surface anticyclone (blue dots) with various
906 surface stress directions in the 15 days after the surface stress is applied in RestartH_{strat}30 experiments. Eddy
907 positions predicted by the kinematic model in equation (10) are shown as circles. The black arrow shows the
908 direction of the surface stress and the green arrow shows the direction of the Ekman flow. Dots are shown at 0.5
909 day intervals.